



Cite this: *Phys. Chem. Chem. Phys.*,
2018, 20, 22168

Hexagonal Ti_2B_2 monolayer: a promising anode material offering high rate capability for Li-ion and Na-ion batteries[†]

Tao Bo,^{ab} Peng-Fei Liu,^{ID ab} Juping Xu,^{ab} Junrong Zhang,^{ab} Yuanbo Chen,^{ab} Olle Eriksson,^c Fangwei Wang^{abd} and Bao-Tian Wang ^{ID *ab}

Combining the first-principles density functional method and crystal structure prediction techniques, we report a series of hexagonal two-dimensional transition metal borides including Sc_2B_2 , Ti_2B_2 , V_2B_2 , Cr_2B_2 , Y_2B_2 , Zr_2B_2 , and Mo_2B_2 . Their dynamic and thermal stabilities are testified by phonon and molecular dynamics simulations. We investigate the potential of the two-dimensional Ti_2B_2 monolayer as an anode material for Li-ion and Na-ion batteries. The Ti_2B_2 monolayer possesses high theoretical specific capacities of 456 and 342 mA h g⁻¹ for Li and Na, respectively. The very high Li/Na diffusivity with an ultralow energy barrier of 0.017/0.008 eV indicates an excellent charge-discharge capability. In addition, good electronic conductivity during the whole lithiation process is found by electronic structure calculations. The very small change in volume after the adsorption of one, two, and three layers of Li and Na ions indicates that the Ti_2B_2 monolayer is robust. These results highlight the suitability of Ti_2B_2 monolayer as well as the other two-dimensional transition metal borides as excellent anode materials for both Li-ion and Na-ion batteries.

Received 27th May 2018,
Accepted 3rd August 2018

DOI: 10.1039/c8cp03362e

rsc.li/pccp

1. Introduction

Research on advanced energy storage technology is significant for the development of modern society.¹ Rechargeable lithium-ion batteries (LIBs), one of the widely studied clean energy-storage technologies, have attracted increasing attention due to the combination of outstanding reversible capacity, high power density, superior energy efficiency, long cycle life, and portability.^{2–9} Currently, LIBs are widely applied in portable electronics, electric vehicles, and electricity grid systems.^{10,11} In addition to LIBs, an alternative option is the rechargeable Na-ion batteries (NIBs),

which have been found to be promising and could be a good candidate to replace LIBs in the future because sodium is more abundant and cheaper than lithium.^{12–16} The capability of LIBs and NIBs is highly dependent on the performances of their electrode materials.^{17,18} Nowadays, graphite is commercially used as an anode material for LIBs because of its high coulombic efficiency, relatively good cycling stability, and low cost,^{19,20} but the relatively low theoretical specific capacity (372 mA h g⁻¹) and poor rate capability restrict its further application.²¹ In addition, graphite cannot be used in NIBs, because the Na-C interaction is found to be too weak to contribute to the necessary Coulomb interactions.²² Therefore, new anode materials to further improve the performance of LIBs and NIBs are urgently needed.^{23–25}

Two-dimensional (2D) materials^{26–29} are of special interest as anode materials for LIBs and NIBs because of their high surface area, remarkably high electron mobility and superior mechanical properties.³⁰ In recent years, many 2D materials have been investigated as anode materials and great success has been obtained.^{31–48} Graphene represents the first example of a 2D electrode material for LIBs.^{49,50} Since then, novel 2D materials including MoS₂,⁵¹ VS₂,⁵² silicene,⁵³ phosphorene,^{54–56} borophene,^{31,57} borophane,³⁷ boron phosphide,³⁸ Mo₂C,⁴⁰ and so on have been investigated as anode materials for LIBs or NIBs. In addition, 2D transition metal carbides or nitrides, called MXenes,^{58,59} have also attracted great interest in this field.^{32–34}

^a Institute of High Energy Physics, Chinese Academy of Science (CAS), Beijing 100049, China. E-mail: wangbt@ihep.ac.cn

^b Dongguan Neutron Science Center, Dongguan 523803, China

^c Department of Physics and Astronomy, Division of Materials Theory, Uppsala University, Box 516, SE-75120 Uppsala, Sweden

^d Beijing National Laboratory for Condensed Matter Physics, Institute of Physics, Chinese Academy of Sciences, Beijing 100080, China

[†] Electronic supplementary information (ESI) available: (I) Computational method, (II) metastable isomers of 2D Ti_2B_2 , (III) lattice constants (Å) of the bulk TMB₂ phases and the 2D TM₂B₂ structures, (IV) DOS and phonon dispersion curves of the other six 2D TM₂B₂, (V) snapshots and variation of the free energy and RDFs for 2D Ti_2B_2 in the AIMD simulations from 300 to 3000 K, (VI) charge density difference plots for Na adsorption, (VII) adsorption structures of Li/Na with various concentrations on Ti_2B_2 , (VIII) 2D TiB₄ structures and the adsorption and diffusion of Li/Na on the hexagonal TiB₄ monolayer, (IX) intercalation of Li/Na in bilayers of Ti_2B_2 . See DOI: 10.1039/c8cp03362e

MXenes can be synthesized by selective etching of A atoms from MAX phases with hydrofluoric acid (HF) at room temperature^{58,59} and the advantage of easy fabrication offers an intrinsic potential for their practical applications.^{58,60–63} Although many 2D materials have been confirmed theoretically as potential electrode materials, the search for LIBs and NIBs with better performance is still necessary and significant. Very recently, Guo *et al.*⁶⁴ investigated new 2D transition metal borides (TMBs) such as Fe₂B₂ and Mo₂B₂ for LIBs. As far as we know, this is the first time that 2D TMBs have been investigated for LIBs. These 2D TMBs belong to the orthorhombic system and can be obtained from layered orthorhombic TMBs that possess high structural similarity to the MAX phases. In addition to these orthogonal structures, there is also a family of layered TMBs that belong to the hexagonal crystal system with the formula TMB₂. These layered TMBs contain graphene-like honeycomb boron layers and can be transformed into 2D “sandwich” structures that consist of two boron honeycomb sheets and an intermediate hexagonal plane of the TM atom (B-TM-B).^{65,66} However, because the outermost sheets of MXenes are composed of metallic atoms, we are interested in whether the hexagonal TMBs can also be transformed into a 2D structure consisting of an intermediate boron honeycomb and two outer hexagonal planes of TM atoms (TM-B-TM). Besides, we are greatly interested in investigating the potential applications of these 2D materials as LIBs and NIBs.

In this work, we first report a series of 2D TMBs including Sc₂B₂, Ti₂B₂, V₂B₂, Cr₂B₂, Y₂B₂, Zr₂B₂, and Mo₂B₂. This monolayer TM₂B₂ belongs to the space group *P6/mmm* with 4 atoms in a hexagonal unit cell, which is identified as consisting of an intermediate boron honeycomb sheet sandwiched in between two hexagonal planes of TM atoms. These 2D TMBs can be produced from their bulk phase, which is a family of layered TMBs of the hexagonal crystal system with the formula TMB₂. Furthermore, we chose Ti₂B₂ as a representative and investigated its performance as an anode material for LIBs and NIBs by performing first-principles calculations. Our results illustrate that Ti₂B₂ monolayer is a promising electrode material for LIBs and NIBs. This fact is encouraging and indicates that our predicted series of 2D TMBs could be promising candidates for next-generation portable batteries.

2. Computational method

The particle-swarm optimization (PSO) scheme, as implemented in the CALYPSO code,^{67–69} was employed to search for low energy 2D Ti₂B₂ structures. The underlying energy calculations and structure optimizations were performed by using the plane-wave-based density-functional theory (DFT) method as implemented in the Vienna ab-initio Simulation Package (VASP).^{70–72} The computational details of the PSO and DFT methods are illustrated in the ESI.† The adsorption energy of lithium and sodium atoms on the Ti₂B₂ monolayer is obtained from:

$$E_{\text{ad}} = (E_{\text{MTi}_2\text{B}_2} - E_{\text{Ti}_2\text{B}_2} - nE_{\text{M}})/n \quad (\text{M} = \text{Li, Na}) \quad (1)$$

where $E_{\text{MTi}_2\text{B}_2}$ and $E_{\text{Ti}_2\text{B}_2}$ represent the total energies of the metal-ion adsorbed monolayer system and the isolated monolayer,

respectively, and E_{M} represents the total energy per atom for the bulk metal. The charge density difference $\Delta\rho$ is calculated based on the following equation:

$$\Delta\rho = \rho_{\text{MTi}_2\text{B}_2} - \rho_{\text{Ti}_2\text{B}_2} - \rho_{\text{M}} \quad (\text{M} = \text{Li, Na}) \quad (2)$$

where $\rho_{\text{MTi}_2\text{B}_2}$, $\rho_{\text{Ti}_2\text{B}_2}$, and ρ_{M} are the total charge of the Li/Na adsorbed system, the Ti₂B₂ monolayer, and the Li/Na atom, respectively. To assess the adsorption stability of the Li/Na layer on the Ti₂B₂ monolayer, the average adsorption energies for each Li/Na layer are calculated according to the following equation:

$$E_{\text{ave}} = (E_{\text{M}_n\text{Ti}_2\text{B}_2} - E_{\text{M}_{(n-1)}\text{Ti}_2\text{B}_2} - mE_{\text{M}})/m \quad (\text{M} = \text{Li, Na}) \quad (3)$$

where $E_{\text{M}_n\text{Ti}_2\text{B}_2}$ and $E_{\text{M}_{(n-1)}\text{Ti}_2\text{B}_2}$ are the total energies of 2D Ti₂B₂ with n and $(n-1)$ adsorbed Li/Na layers, and E_{M} stands for the total energy per atom for the bulk metal. The number m represents m adsorbed Li/Na atoms in each layer (for a 2×2 supercell on both sides). The formation energy for all M_xTi₂B₂ (M = Li, Na) compounds with respect to Ti₂B₂ and Li/Na bulk metal as the reference states is calculated based on the following equation:

$$E_{\text{f}}(x) = (E_{\text{M}_x\text{Ti}_2\text{B}_2} - E_{\text{Ti}_2\text{B}_2} - xE_{\text{M}})/(x+1) \quad (\text{M} = \text{Li, Na}) \quad (4)$$

where $E_{\text{M}_x\text{Ti}_2\text{B}_2}$ is the energy of the M_xTi₂B₂ compound per Ti₂B₂ formula unit, $E_{\text{Ti}_2\text{B}_2}$ is the energy of Ti₂B₂ per Ti₂B₂ formula unit, and E_{M} is the energy per atom of M in the bulk metal. The theoretical capacity can be obtained from:

$$C_{\text{A}} = czF/M_{\text{Ti}_2\text{B}_2} \quad (5)$$

where c is the number of adsorbed Li/Na ions, z is the valence number of Li/Na, F is the Faraday constant (26 801 mA h mol⁻¹), and $M_{\text{Ti}_2\text{B}_2}$ is the molar weight of Ti₂B₂. For every concentration x of the M_xTi₂B₂ compound, the electrode potential V with respect to M/M⁺ is calculated as:⁷³

$$V = -\frac{E(x_2) - E(x_1) - (x_2 - x_1)E(\text{M})}{e(x_2 - x_1)} \quad (\text{M} = \text{Li, Na}) \quad (6)$$

where $E(x_2)$ and $E(x_1)$ are the total energies of M_xTi₂B₂ at two adjacent concentrations x_2 and x_1 , and $E(\text{M})$ is the energy per atom of Li/Na in the bulk metal.

3. Results and discussion

3.1 2D TM₂B₂ and bulk TMB₂.

Motivated by the excellent performance of the MXenes in energy storage,⁷⁴ we investigate TM-B systems characterized by 2D “sandwich” structures. Interestingly, through structural prediction by using the CALYPSO code, we find several 2D Ti₂B₂ structures. The global minimum structure is shown in Fig. 1a and the other metastable isomers are shown in Fig. S1 in the ESI.† The obtained orthorhombic 2D Ti₂B₂ monolayer (Fig. S1a, ESI†) possesses the same structure as those of 2D Fe₂B₂ and Mo₂B₂ reported by Guo *et al.*⁶⁴ According to our calculations, the energy of this orthorhombic 2D Ti₂B₂ monolayer is higher by 0.067 eV per atom than that of the obtained hexagonal 2D Ti₂B₂, which is the global minimum structure (Fig. 1a).

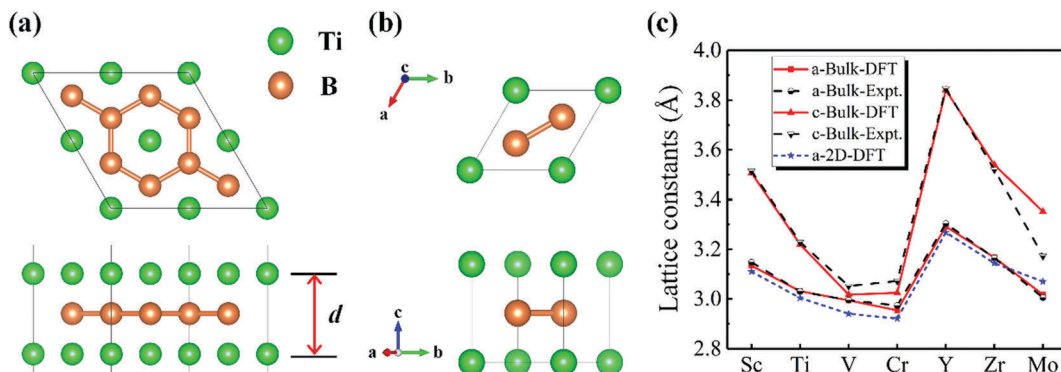


Fig. 1 Top and side views of (a) global minimum phase of Ti_2B_2 monolayer and (b) bulk Ti_2B_2 . The Ti and B atoms are denoted by green and orange spheres, respectively. (c) Lattice constants of the bulk TMB_2 phase and the 2D TM_2B_2 structure.

This hexagonal 2D Ti_2B_2 consists of an intermediate boron honeycomb sheet sandwiched in between two hexagonal planes of Ti atoms. Each boron atom bonds to three boron neighbors and the calculated B-B bond length is 1.734 Å. The line charge density distribution along the B-B bond is 0.121 e per a.u.³, which is larger than the value of 0.104 e per a.u.³ found for the Si covalent bond.⁷⁵ This indicates that the B layers are strongly bonded by B-B covalent bonds. Each Ti atom bonds to six B neighbors and the calculated Ti-B bond length is 2.332 Å. The bulk phase of this 2D structure crystallizes in the hexagonal $P6/mmm$ space group (AlB₂ type No. 191) with $N = 3$ in the unit cell stacked along the c -axis (see Fig. 1b). The atomic Wyckoff positions of bulk Ti_2B_2 are: Ti in 1a (0,0,0) and B in 2d (1/3,2/3,1/2).⁷⁶ As far as we know, many hexagonal bulk TMB_2 structures have been synthesized and all are confirmed to possess layered structural properties.^{77–80} Thus, we further investigated the viability in other 2D TM_2B_2 monolayers. By substituting the

Ti atom in 2D Ti_2B_2 with other TM atoms, we found that the hexagonal 2D TM_2B_2 geometry can be maintained for $\text{TM} = \text{Sc}, \text{V}, \text{Cr}, \text{Y}, \text{Zr}, \text{Mo}$.

The optimized lattice constants (both a and c) of these bulk TMB_2 are shown in Fig. 1c and Table S1 in the ESI,[†] and they are consistent with the experimental results reported earlier.^{76–79,81} The optimized lattice constant of 2D Ti_2B_2 is $a = b = 3.004$ Å, which is comparable to that of bulk Ti_2B_2 (3.031 Å).⁷⁶ The optimized thickness of 2D Ti_2B_2 is $d = 3.117$ Å, also comparable to the lattice constant c of bulk Ti_2B_2 (3.220 Å).⁷⁶ As shown in Fig. 1c, the optimized lattice constant (a) values of the other six 2D TM_2B_2 are all consistent with those of their corresponding bulk structures.

As shown in Fig. 2a, 2D Ti_2B_2 exhibits a metallic property contributed mainly by the Ti-3d orbitals. The contribution from B-2p is ignorable. The TDOS and PDOS of 2D Sc_2B_2 , V_2B_2 , Cr_2B_2 , Y_2B_2 , Zr_2B_2 , and Mo_2B_2 (shown in Fig. S2 in the ESI[†]) indicate

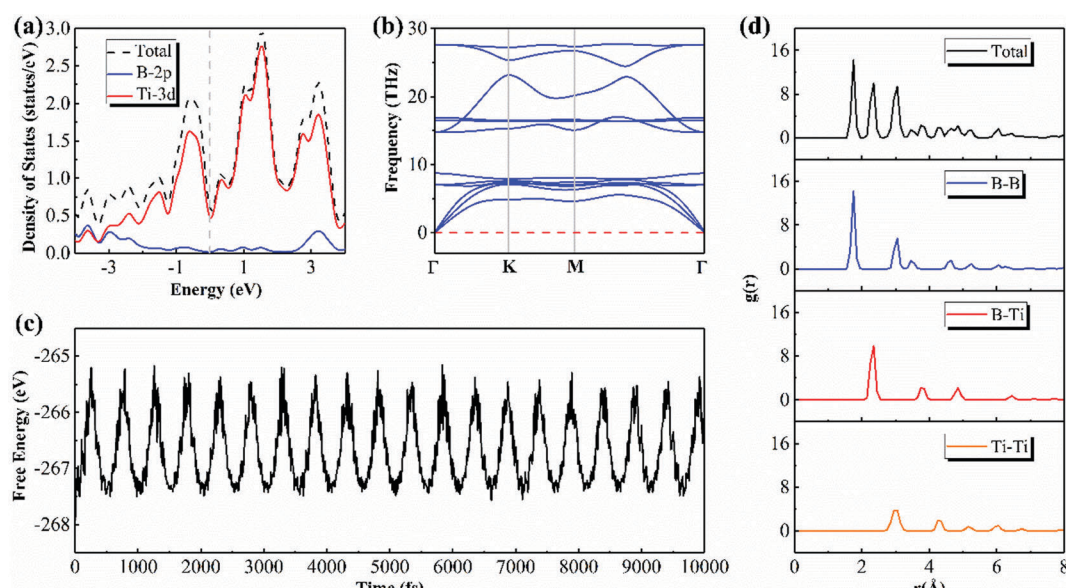


Fig. 2 (a) Total and partial density of states (TDOS and PDOS) of 2D Ti_2B_2 . The dashed black line represents the TDOS while the solid red and solid blue lines stand for the Ti-3d and B-2p PDOS, respectively. The Fermi energy level is set at zero. (b) Phonon dispersion curves of the 2D Ti_2B_2 . (c) Variation of the free energy in the AIMD simulations at 300 K over the time scale of 10 ps. (d) Radius distribution function (RDF) of 2D Ti_2B_2 at 300 K.

that these six 2D materials, like 2D Ti_2B_2 , present good conductivity. Owing to the outstanding electronic conductivity of these 2D TM_2B_2 , they merit potential application as anode materials for LIBs and NIBs.

The stability of anode materials is the most fundamental and critical factor in their practical applications. To examine the dynamic stability of 2D Ti_2B_2 , we calculated its phonon dispersion curves. As shown in Fig. 2b, the absence of imaginary modes in the whole BZ confirms that 2D Ti_2B_2 is dynamically stable. The highest frequency of 2D Ti_2B_2 reaches up to 27.725 THz (924 cm^{-1}), which is higher than those of FeB_2 (854 cm^{-1}),⁸² TiC (810 cm^{-1}),⁸³ Cu_2Si (420 cm^{-1}),⁸⁴ and MoS_2 (473 cm^{-1})⁸⁵ monolayers. The high value of frequencies in the phonon dispersion also indicates the stability of this 2D material. The phonon spectra of the other six 2D TM_2B_2 were also calculated and they are shown in Fig. S3 in the ESI.[†] We find that these 2D TM_2B_2 are also dynamically stable. To check the thermal stability, we carried out AIMD simulations for 2D Ti_2B_2 at temperatures of 300, 600, 1200, 1800, 2400, and 3000 K, respectively. At 300 K, the average value of free energy remains almost constant during the whole simulation (see Fig. 2c), confirming that 2D Ti_2B_2 is thermally stable at room temperature. Even on increasing the temperature up to 2400 K, the original geometry remains intact with only slight in-plane and out-of-plane deformations (see Fig. S4, ESI[†]). The free energies fluctuate around constant values during the AIMD simulation below and at 2400 K (see Fig. S5, ESI[†]). The pair correlation function was also calculated at 300, 600, 1200, 1800, 2400, and 3000 K, respectively. At 300 K, the RDF (radius distribution function) between 1 and 6 Å has many peaks, indicating the long range order of this material after annealing (see Fig. 2d). Even on increasing the temperature up to 2400 K, there are peaks between 1 and 6 Å (see Fig. S6, ESI[†]). However, at higher temperatures such as 3000 K, RDF peaks broaden and merge together (see Fig. S6, ESI[†]). These results confirm that 2D Ti_2B_2 is stable upon heating, which is a safeguard for practical applications.

3.2 Adsorption of Li and Na on the 2D Ti_2B_2 monolayer

Next, we investigated the adsorption behaviors of Li/Na atoms on the Ti_2B_2 monolayer. We first investigated the adsorption behaviors of a single Li/Na atom on the surface of 2D Ti_2B_2 by considering three high symmetry adsorption sites S1, S2, and S3 (see Fig. 3a). The adsorption energies of the Li/Na atom on these sites are shown in Fig. 3b. We find that the Na-adsorbed configurations are more stable than the Li-adsorbed ones and S1 is always the most stable adsorption site for both Li and Na atoms. Interestingly, the adsorption energies on S3 are very close to those on S1, suggesting that the Li/Na atoms easily diffuse along the S1–S3–S1 direction, *i.e.* the B–B bonding direction. The adsorption energies on S2 are larger by 0.06–0.13 eV than those on S1 and S3. This indicates that it is not possible for the Li/Na atom to appear on top of the Ti atoms. To better understand the adsorption properties of Li/Na on the Ti_2B_2 surface, we calculated the difference charge density and we present the results in Fig. 4 (Li-adsorption) and Fig. S7 (Na-adsorption) (ESI[†]). It is clear that the electrons tend to accumulate in

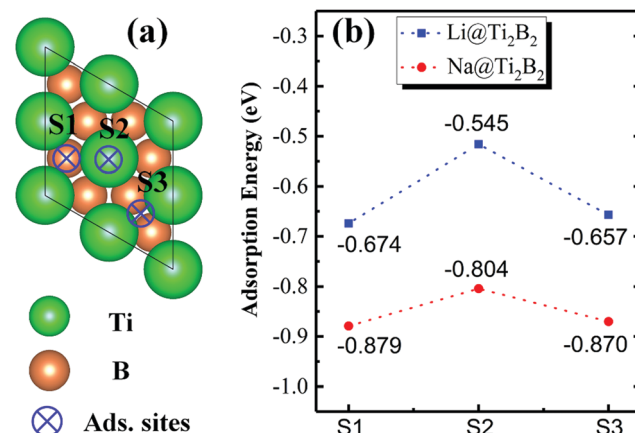


Fig. 3 (a) High symmetry adsorption sites and (b) adsorption energies for Li/Na on the surface of 2D Ti_2B_2 . The Ti and B atoms are denoted by green and orange spheres, respectively.

between Li/Na and its neighboring Ti atoms, thus resulting in Li/Na–Ti bonding. This chemical bonding between Li/Na atoms and 2D Ti_2B_2 is favorable to prevent the forming of Li/Na clusters and improve the safety and application availability for Li/Na storage in LIBs and NIBs.

3.3 Theoretical specific capacity and voltage profile

For practical application, it is of great significance to investigate the storage capacity of the batteries that use the electrode materials. Thus, the average adsorption energies were calculated to investigate the storage capacity of Li/Na on the Ti_2B_2 monolayer. The adsorptions of one, two, and three layers of Li on both sides of the Ti_2B_2 monolayer were investigated using 2×2 supercells and can be labeled as $\text{Li}_x\text{Ti}_2\text{B}_2$ with $x = 2, 4$ and 6 , respectively. For the one-layer adsorption, shown in Fig. 5a, all Li atoms are adsorbed at the S1 sites. Under conditions of saturation, there are eight Li atoms that can be adsorbed on both sides of the Ti_2B_2 monolayer. The average adsorption energy of the Li atoms is -0.526 eV , which indicates that Li adatoms can be

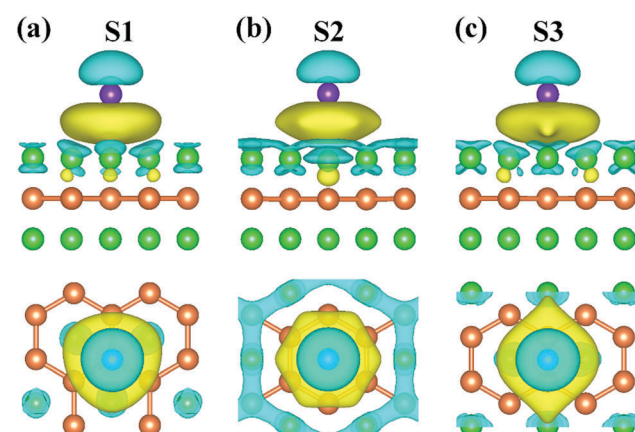


Fig. 4 The charge density difference plots for Li adsorption on the (a) S1, (b) S2, and (c) S3 sites of 2D Ti_2B_2 monolayer. The yellow and cyan areas represent electron gains and losses. The Ti, B, and Li atoms are denoted by green, orange, and violet spheres, respectively.

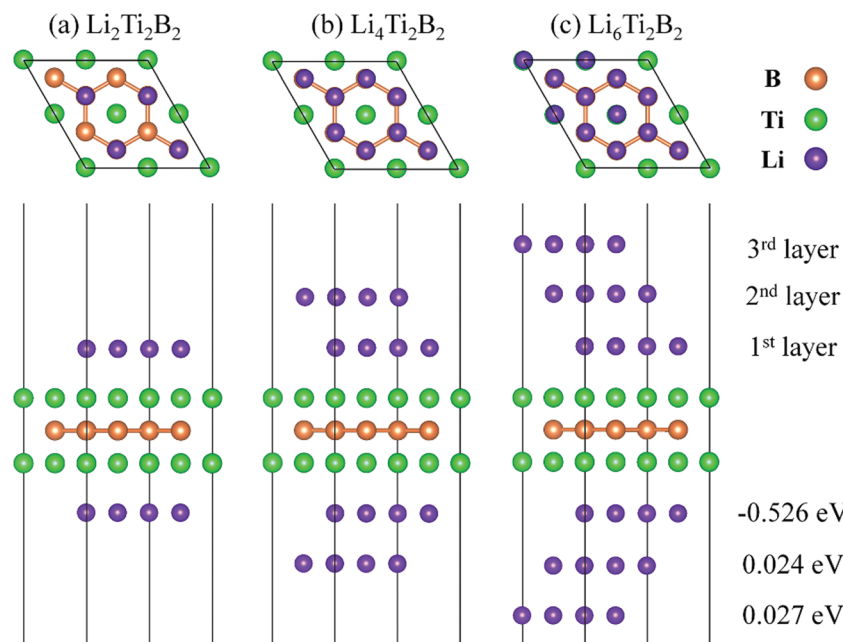


Fig. 5 Top and side views of the structures of (a) $\text{Li}_2\text{Ti}_2\text{B}_2$, (b) $\text{Li}_4\text{Ti}_2\text{B}_2$, and (c) $\text{Li}_6\text{Ti}_2\text{B}_2$ with layers of Li ions adsorbed on the surface of the 2D Ti_2B_2 monolayer. The Ti, B, and Li atoms are denoted by green, orange, and violet spheres, respectively.

adsorbed stably without clustering. After the first layer is adsorbed fully, the subsequently added Li atoms will form the second adsorbed layer. The Li atoms are also adsorbed at the S1 sites (see Fig. 5b). This can be regarded as two-layer adsorption and there are 16 Li atoms being adsorbed in the condition of full adsorption. For the three-layer adsorption, the third-layer Li atoms are adsorbed at the S2 sites (Fig. 5c). In the condition of full adsorption, there are 24 Li atoms being adsorbed. The adsorption energies for one-layer, two-layer, and three-layer adsorption are -4.208 , -4.019 , and -3.800 eV, respectively. However, according to eqn (3), the calculated average adsorption energies for the second and third layers of Li atoms are 0.024 and 0.027 eV, respectively. The positive values of these adsorption energies mean that the adsorptions of two and three layers of Li are not energetically stable. The above results reveal that the 2×2 supercell of the Ti_2B_2 monolayer can accumulate 8 Li atoms at most, corresponding to $\text{Li}_2\text{Ti}_2\text{B}_2$ with a symmetric configuration of adatoms on both sides of the Ti_2B_2 monolayer.

Next, we turn our focus onto the case of the Na-adsorbed Ti_2B_2 system. The one-layer, two-layer, and three-layer adsorptions of Na on both sides of 2D Ti_2B_2 were calculated and the corresponding schematic pictures are presented in Fig. 6. For clarity, only Na atoms on a single side of 2D Ti_2B_2 are shown in this figure. The first layer can accommodate at most six Na atoms on both sides of the Ti_2B_2 monolayer, three Na atoms on each side. This number is less than that of Li adsorption. Since the atomic radius of Na is larger than that of Li, this fact is understandable. As shown in Fig. 6a, the three Na atoms form an equilateral triangle and the adsorption sites are not S1. When the first layer is adsorbed fully, the additionally added Na atoms will form the second layer at sites above the center of the equilateral triangles (Fig. 6b). The adsorption sites for the

third layer are above the center of the equilateral triangles of the second layer (Fig. 6c). The second and the third layers can also accommodate as many as six Na atoms on both sides. The average adsorption energies are all negative for the first, the second, and the third layers (-0.502 , -0.007 , and -0.009 eV, respectively), indicating that Na atoms can be adsorbed stably without clustering. Furthermore, the adsorption of four layers of Na on the Ti_2B_2 monolayer is not energetically stable according to our calculation. Although the adsorption energies are negative for the second and third layers, they are too small. These small adsorption energies are actually meaningless because the calculations are done at 0 K. Besides, a much larger spacing is needed between the Ti_2B_2 monolayers to accommodate multilayer adsorptions. On the basis of these results, we can conclude that the 2×2 supercell of Ti_2B_2 monolayer can accommodate 6 Na adatoms, corresponding to $\text{Na}_{1.5}\text{Ti}_2\text{B}_2$.

According to eqn (4), we calculated the formation energies of $\text{Li}_x\text{Ti}_2\text{B}_2/\text{Na}_x\text{Ti}_2\text{B}_2$ with respect to Ti_2B_2 and Li/Na bulk metal over a large composition range for the most stable adsorption configurations (see Fig. 7). We also present a convex hull for the formation energies (blue line). The convex hull is the formation energy *versus* composition curve and it is the set of lines that connects the lowest energy ordered phases. Structures located on the hull are thermodynamically stable relative to dissociation into other configurations, while those above the hull are metastable. The stable adsorption configurations are presented in Fig. S8 and S9 (ESI†). As shown in Fig. 7a, the compounds of $\text{Li}_x\text{Ti}_2\text{B}_2$ ($x = 0.25, 0.5, 1.0, 2.0$) lie on the convex hull, while the compounds of $\text{Li}_{4.0}\text{Ti}_2\text{B}_2$ and $\text{Li}_{6.0}\text{Ti}_2\text{B}_2$ lie above the convex hull. This also indicates that the adsorptions of two and three layers of Li on Ti_2B_2 are not stable in energy. Fig. 7b shows that the compounds of $\text{Na}_x\text{Ti}_2\text{B}_2$ ($x = 0.25, 0.5, 1.0, 1.5$) all lie on the

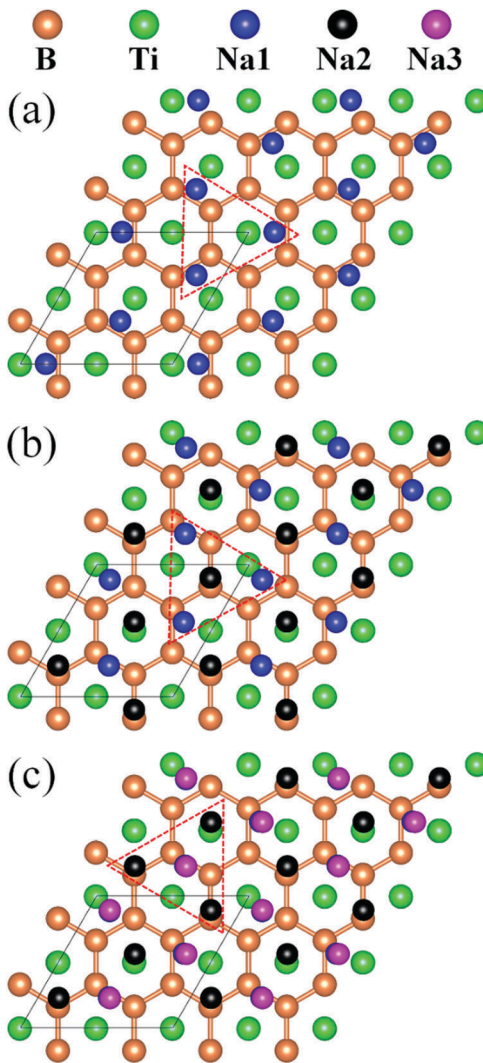


Fig. 6 Top views of (a) one-layer, (b) two-layer, and (c) three-layer adsorptions of Na ions on the 2D Ti_2B_2 monolayer. Na1, Na2, and Na3 represent the Na ions adsorbed in the first, the second, and the third layer, respectively. The black lines stand for the range of a 2×2 supercell.

convex hull, indicating that the compounds of $\text{Na}_{0.25}\text{Ti}_2\text{B}_2$, $\text{Na}_{0.5}\text{Ti}_2\text{B}_2$, $\text{Na}_{1.0}\text{Ti}_2\text{B}_2$, and $\text{Na}_{1.5}\text{Ti}_2\text{B}_2$ are all stable. According to these results and eqn (5), the theoretical specific capacities of 2D Ti_2B_2 as an electrode for LIBs and NIBs are ~ 456 and 342 mA h g^{-1} , respectively.

Fig. 8 shows the concentration-dependent profile of the electrode potential for both Li-intercalated and Na-intercalated Ti_2B_2 . The x values are selected along the calculated convex hull shown in Fig. 7. As shown in Fig. 8a, we find that the electrode potential of Li-intercalated Ti_2B_2 varies in the range of 0.473–0.674 V with a decreasing trend with increasing capacity. There are four main plateaus. The initial plateau shows a voltage of 0.674 V vs. Li/Li^+ corresponding to the lithium concentration varying from $x = 0$ to 0.25. The second and third plateaus show voltages of 0.599 V from $x = 0.25$ to 0.50 and 0.522 V from $x = 0.50$ to 1.0, respectively. The fourth plateau, $\text{Li}_{1.0}\text{Ti}_2\text{B}_2 \rightarrow \text{Li}_{2.0}\text{Ti}_2\text{B}_2$, displays a voltage of 0.473 V vs. Li/Li^+ . The average value of the

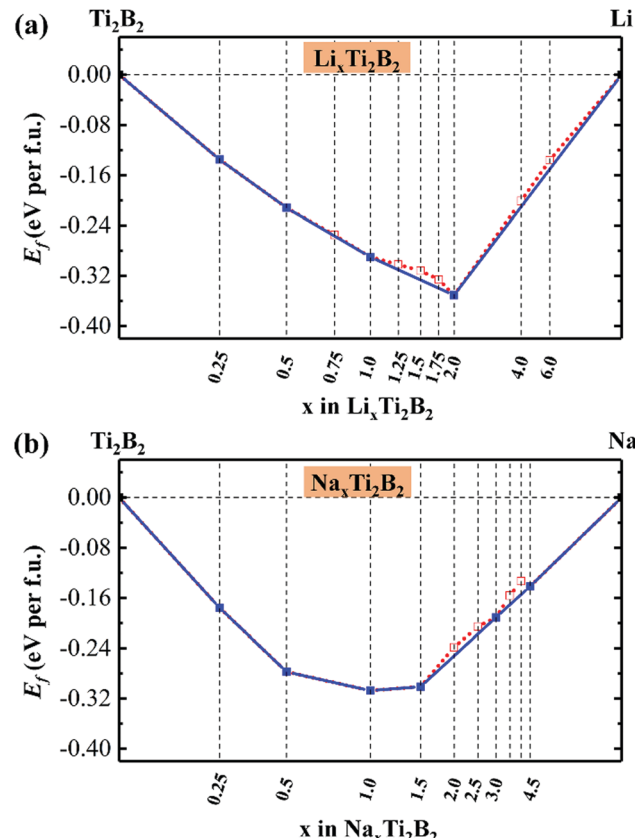


Fig. 7 Formation energies of (a) $\text{Li}_x\text{Ti}_2\text{B}_2$ and (b) $\text{Na}_x\text{Ti}_2\text{B}_2$ systems with respect to 2D Ti_2B_2 and Li/Na bulk metal. Data points located on the convex hull (solid squares) represent stable adsorption against any type of decomposition. The metastable phases are indicated by open squares.

electrode potential is 0.526 V vs. Li/Li^+ . The plotted voltage profile for the Na insertion is shown in Fig. 8b. We find that the voltage profile of Na-intercalated Ti_2B_2 varies in a broader range of 0.277–0.879 V. There are four main plateaus that correspond to $\text{Ti}_2\text{B}_2 \rightarrow \text{Na}_{0.25}\text{Ti}_2\text{B}_2$, $\text{Na}_{0.25}\text{Ti}_2\text{B}_2 \rightarrow \text{Na}_{0.5}\text{Ti}_2\text{B}_2$, $\text{Na}_{0.5}\text{Ti}_2\text{B}_2 \rightarrow \text{Na}_{1.0}\text{Ti}_2\text{B}_2$, and $\text{Na}_{1.0}\text{Ti}_2\text{B}_2 \rightarrow \text{Na}_{1.5}\text{Ti}_2\text{B}_2$, respectively. The voltages of these four plateaus are 0.879, 0.786, 0.397, and 0.277 V, respectively, and the average value is 0.502 eV. Since a good anode should have a low electrode potential, our calculated voltage profile in Fig. 8 suggests that 2D Ti_2B_2 is suitable as an anode for LIBs and NIBs.

We also estimated the variation of the lattice constant and thickness of the Ti_2B_2 monolayer after the adsorption of layered Li/Na atoms. The lattice constant increases from 6.008 (Ti_2B_2) to 6.047 Å ($\text{Ti}_2\text{B}_2\text{Li}_2$) for Li adsorption (about 0.65% tensile strain) and from 6.008 (Ti_2B_2) to 6.040 ($\text{Ti}_2\text{B}_2\text{Na}_{1.5}$) for Na adsorption (about 0.53% tensile strain). The calculated thickness of the Ti_2B_2 monolayer for the one-layer adsorbed Li structure ($\text{Ti}_2\text{B}_2\text{Li}_2$) is 3.128 Å, which is larger by 0.29% than that of the bare monolayer (3.119 Å). However, the thickness of the Ti_2B_2 monolayer for the one-layer ($\text{Ti}_2\text{B}_2\text{Na}_{1.5}$) adsorption of Na is 3.108 Å, which is smaller by 0.35% than the bare one. In view of these results, the Ti_2B_2 monolayer is robust for use as an anode material in both LIBs and NIBs.

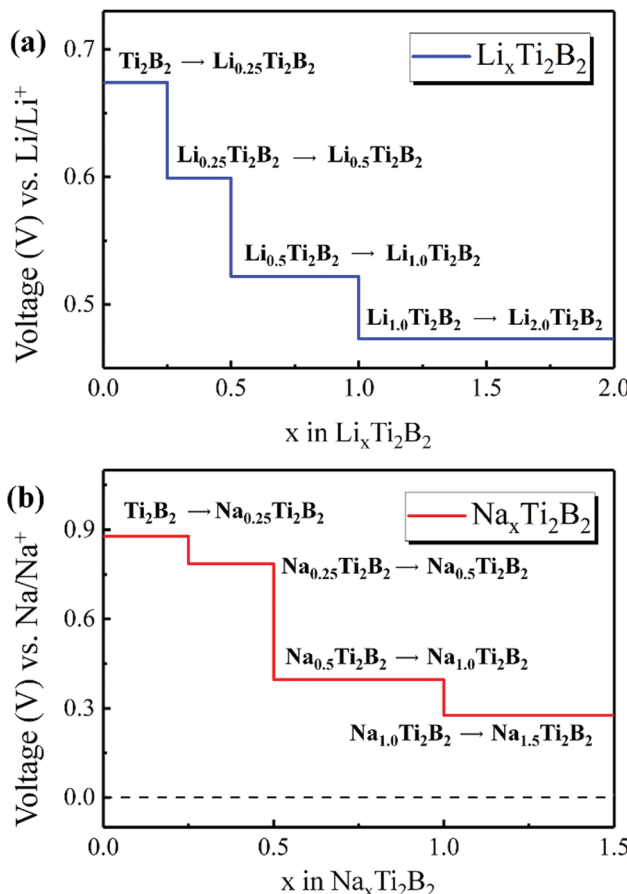


Fig. 8 Electrode potential of (a) Li-intercalated Ti_2B_2 against Li/Li^+ and (b) Na-intercalated Ti_2B_2 against Na/Na^+ .

3.4 Electronic structures of the 2D Ti_2B_2 monolayer with adsorbed Li/Na atoms

It is well known that electronic conductivity is closely associated with the rate capability of the anode materials in LIBs and NIBs. Unlike many other 2D materials that exhibit semi-conducting or semi-metallic characteristics,^{86,87} our previous analyses have demonstrated that the pristine Ti_2B_2 monolayer exhibits intrinsic metallic behavior. In order to gain insight into the electronic conductivity of the charge–discharge process, the evolutions of DOS for Ti_2B_2 monolayer adsorbed with Li/Na atoms were calculated (Fig. 9). Fig. 9a shows the DOS of a single Li adsorbed on the Ti_2B_2 monolayer. Compared to the DOS of the pristine Ti_2B_2 monolayer (Fig. 2a), we find that the orbital contributions around the Fermi level mainly come from the sheet but with negligible components from the Li atoms, endowing the system with a metallic characteristic. It should be mentioned that the Ti_2B_2 monolayer is easily terminated with multiple Li atoms, hence the modulation effect of surface atomic number on electronic structures was also evaluated in one layer (Fig. 9b) of adsorbed Li configurations. With the Li concentration increasing during the charging process, the orbital contributions from Li atoms near the Fermi level increase. However, the components of the monolayer show no big fluctuations. These simulations explicitly demonstrate that the system

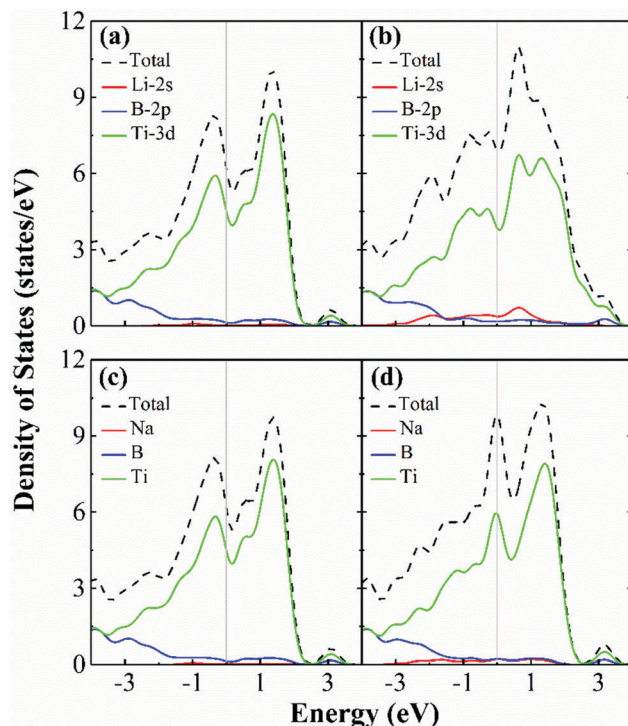


Fig. 9 TDOS and PDOS of the 2D Ti_2B_2 monolayer adsorbed with (a) one Li atom, (b) one layer of Li atoms, (c) one Na atom, and (d) one layer of Na atoms, respectively. The Fermi energy levels are set as zero.

retains its metallic nature during the Li atomic adsorption process. Similar evolutions of DOS for the host Ti_2B_2 monolayer with one Na and one layer of Na adsorbed are also shown in Fig. 9. These robust electronic properties of the Ti_2B_2 monolayer greatly expand its potential applications in anode materials and will motivate subsequent experimental studies.

3.5 Li/Na diffusion on 2D Ti_2B_2 monolayer

In addition to the high specific capacity, a good charge–discharge rate capability is of great significance for a promising anode material for LIBs and NIBs. The diffusion barrier of Li/Na is a key factor that determines the charge–discharge rate. In this part, we employ the CI-NEB method to investigate the diffusion barriers for Li and Na atoms on the surface of the Ti_2B_2 monolayer. As Li and Na atoms preferentially occupy the S1 site, one possible pathway starting from one S1 site to another S1 site is considered. This pathway is from A to B (Fig. 10a) and is connected by four S1 and three S3 sites. It can be viewed as S1–S3–S1–S3–S1–S3–S1. As illustrated in Fig. 10b, the energy barrier for Li diffusion along the A–B pathway is 0.017 eV while that for Na diffusion is 0.008 eV. The ultralow diffusion energy barriers indicate that Li and Na atoms can diffuse extremely easily on the Ti_2B_2 monolayer. Furthermore, due to the smaller diffusion energy barrier of Na than that of Li, the Na ions are more easily diffused on the Ti_2B_2 monolayer than the Li ions. The larger rate capacity for Na than Li is also found in other 2D materials, such as B_2H_2 ³⁷ and Mo_2C .⁴⁰ Here, the low diffusion energy barriers are due to the small difference

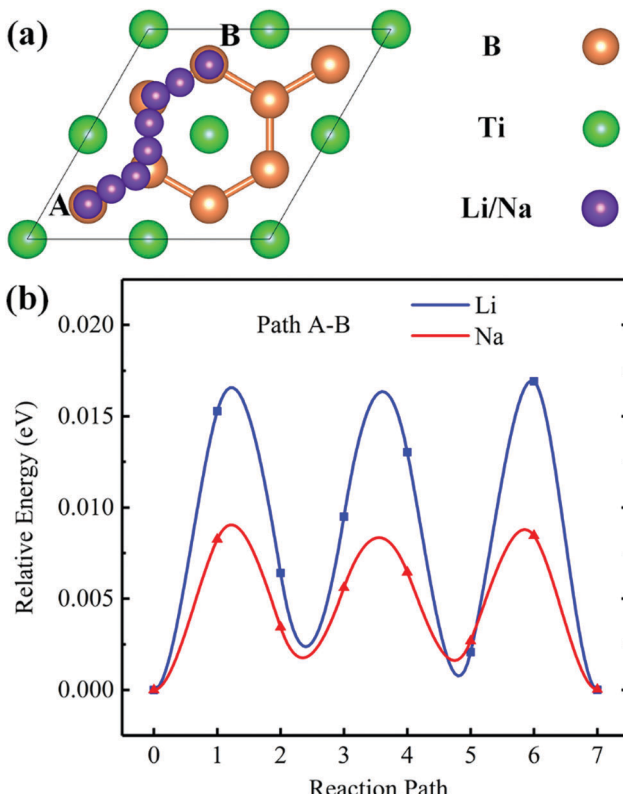


Fig. 10 (a) Top view of the pathway for Li/Na diffusion on the 2D Ti_2B_2 monolayer. The Ti, B, and Li/Na atoms are denoted by green, orange, and violet spheres, respectively. (b) Energy profiles of the corresponding Li and Na diffusion pathways.

of the Li/Na adsorption energies between the S1 and S3 sites. The low diffusion energy barrier for Li/Na ion diffusion would be beneficial to increase the charge–discharge rate of LIBs and NIBs.

To further investigate the diffusion kinetics of Li and Na atoms on the Ti_2B_2 monolayer, AIMD simulations were performed at 300 K lasting for 10 ps. The Li and Na diffusion trajectories during the 10 ps simulation, shown in Fig. 11a and b, respectively, give direct visualizations of the Li and Na diffusion on the Ti_2B_2 monolayer. We see that the Li atom can travel

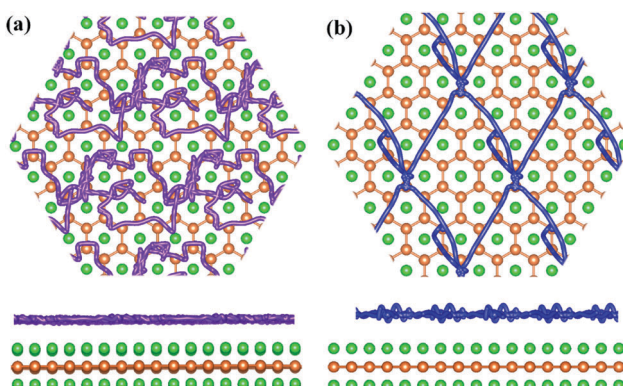


Fig. 11 Top and side views of the calculated (a) Li and (b) Na trajectories during the 10 ps AIMD simulations. The Ti, B, Li, and Na atoms are denoted by green, orange, violet, and blue spheres, respectively.

through the entire region almost freely along the A–B pathway, although the diffusion path is not that straight. Interestingly, the Na atom can diffuse through the entire region in almost straight lines along the A–B pathway. Similar behavior has been observed on borophene for Li diffusion.³¹ The above AIMD simulation results explicitly exhibit an ultra-fast Li/Na diffusion on the 2D Ti_2B_2 monolayer, proving that this 2D material is a promising candidate for high rate LIB and NIB electrode materials.

3.6 Comparison with other anode materials

In order to evaluate the superiority of our studied Ti_2B_2 monolayer as an electrode material for LIBs and NIBs, we compare its theoretical specific capacity and diffusion barrier with those of other widely investigated anode materials^{8,31,33,35–37,40,51–57,64,88–96} in Tables 1 and 2. For Li storage, the theoretical specific capacity of the Ti_2B_2 monolayer is 456 mA h g⁻¹, which is greater than that of well-established graphite,^{8,88,89} phosphorene,^{54,55} Ti_3C_2 ,³³ or $\text{Li}_4\text{Ti}_5\text{O}_{12}$,⁹⁰ and comparable to that of Mo_2C ,⁴⁰ VS_2 ,⁵² B_2H_2 ,³⁷ and planar TiB_4 .⁹⁶ Compared to the orthorhombic 2D MBenes,⁶⁴ the theoretical specific capacity of the hexagonal 2D Ti_2B_2 is in between those of 2D Mo_2B_2 and 2D Fe_2B_2 .⁶⁴ Although the

Table 1 Summary of theoretical specific capacities (mA h g⁻¹) and diffusion barriers (meV) of some widely investigated promising anode materials for LIBs

Species	Theoretical specific capacity	Diffusion barrier	Ref.
Ti_2B_2	456	17	This work
Graphite	372	450–1200	8, 88 and 89
Phosphorene	433	80	54 and 55
Silicon	4200	580	91
Silicene	954	230	53
Sn	994	390	90 and 92
1T- Ti_3C_2	320	70	33
1H- Mo_2C	526	35	40
VS_2	466	220	52
Borophene	1860	2.6	31
B_2H_2	504	210	37
$\text{Li}_4\text{Ti}_5\text{O}_{12}$	175	300	90 and 95
Orthorhombic Fe_2B_2	665	240	64
Orthorhombic Mo_2B_2	444	270	64
Planar TiB_4	588	180	96

Table 2 Summary of theoretical specific capacities (mA h g⁻¹) and diffusion barriers (meV) of some widely investigated promising anode materials for NIBs

Species	Theoretical specific capacity	Diffusion barrier	Ref.
Ti_2B_2	342	8	This work
Phosphorene	865	40	56
Graphene		130	93
Boron-doped graphene	762	160–220	94
1T- MoS_2	146	280	51
1T- Ti_3C_2	352	96	35
1H- Mo_2C	132	15	40
Borophene	496/596	300/12	57
B_2H_2	504	90	37
Ca_2N	1138	80	36
Sr_2N	283	16	36

theoretical specific capacity is lower than that of silicon,⁹¹ silicene,⁵³ and Sn,^{90,92} the energy barrier (0.017 eV) for Li diffusion is the lowest among the listed materials in Table 1 besides borophene.³¹ This indicates that 2D Ti₂B₂ possesses a very high rate capability for Li diffusion.

In the case of Na storage, as shown in Table 2, the theoretical specific capacity of the Ti₂B₂ monolayer is 342 mA h g⁻¹, which is larger than that of MoS₂,⁵¹ Mo₂C,⁴⁰ and Sr₂N,³⁶ and close to that reported in Ti₃C₂.³⁵ It is worth noting that the diffusion energy barrier (0.008 eV) of Na ion on the Ti₂B₂ monolayer is much lower than that of any other typical promising anode materials, shown in Table 2, indicating a very high rate capability.

To access the feasibility of experimental synthesis for 2D Ti₂B₂, we compared the formation energy of 2D Ti₂B₂ with hexagonal 2D TiB₄, whose atomic stacking is B-Ti-B (Fig. S10a, ESI†). The formation energies were investigated with respect to solid Ti and B, $\Delta E(Ti_xB_y) = [E(Ti_xB_y) - xE(Ti) - yE(B)]/(x + y)$, where $E(Ti_xB_y)$ represents the energy of the Ti_xB_y monolayer, and $E(Ti)$ and $E(B)$ represent the energies per atom of the bulk Ti and B, respectively. The calculated formation energy of 2D Ti₂B₂ is -0.195 eV per atom, which is lower by 0.208 eV per atom than that of hexagonal 2D TiB₄ (0.013 eV per atom). This proves that 2D Ti₂B₂ is more stable than hexagonal 2D TiB₄. We also compared the total energy of this hexagonal 2D TiB₄ with the most stable planar 2D TiB₄ structure reported by Qu *et al.*⁹⁶ recently. The calculated total energy of this hexagonal 2D TiB₄ is lower by 0.198 eV per atom than the planar 2D TiB₄ (Fig. S10b, ESI†), indicating the stability of this hexagonal 2D TiB₄. Thus, we calculated the properties of the hexagonal 2D TiB₄ as an anode material for comparison. The most stable adsorption sites and the corresponding adsorption energies are presented in Fig. S11 (ESI†). The 2 × 2 supercell of hexagonal 2D TiB₄ can accommodate 8 Li or Na atoms (Fig. S12, ESI†), corresponding to TiB₄Li₂ and TiB₄Na₂, respectively. The theoretical specific capacity of this hexagonal 2D TiB₄ is 588 mA h g⁻¹ for both Li and Na storage, indicating a higher Li and Na storage than those of 2D Ti₂B₂. However, the diffusion energy barriers of Li (0.712 eV) and Na (0.377 eV) on the hexagonal 2D TiB₄ are much larger than those on 2D Ti₂B₂ (Fig. S13, ESI†), indicating that 2D Ti₂B₂ is more suitable to be an electrode material than 2D TiB₄.

The MXenes are usually covered by a layer of functional groups such as H, F, and O on their surfaces. To better understand the real application of 2D Ti₂B₂, we investigated the Li/Na intercalation energies in a bilayer of Ti₂B₂ with and without functional groups. The intercalation energies were investigated using $E_{\text{intercalation}} = [E(M_xTi_2B_2T) - E(Ti_2B_2T) - xE(M)]/x$ (T = H, O, M = Li, Na), where $E(M_xTi_2B_2T)$, $E(Ti_2B_2T)$, and $E(M)$ are the calculated energies of M_xTi₂B₂T, Ti₂B₂T, and M, respectively. The intercalation energies of Li/Na in bilayers of bare Ti₂B₂, Ti₂B₂H₂, Ti₂B₂H₄, and Ti₂B₂O₂ were calculated. We also calculated the intercalation energies of Li/Na in the bilayer of bare Ti₂C for comparison. All the intercalation energies are listed in Table 3 and the optimized structures are shown in Fig. S14 and S15 (ESI†). The Ti₂B₂ bilayer and the Ti₂C bilayer possess similar intercalation energies of Li/Na, indicating that the

Table 3 Intercalation energies (eV) of Li/Na in bilayers of bare Ti₂C, bare Ti₂B₂, Ti₂B₂H₂, Ti₂B₂H₄, and Ti₂B₂O₂

	Intercalation energy (eV)			
	$x = 0.125$	$x = 0.25$	$x = 0.375$	$x = 0.5$
Li _x Ti ₂ C	2.071	1.675	1.149	0.518
Li _x Ti ₂ B ₂	2.855	2.659	1.345	0.646
Li _x Ti ₂ B ₂ H ₂	2.910	1.148	0.614	0.315
Li _x Ti ₂ B ₂ H ₄	0.747	-1.525	-0.937	-0.519
Li _x Ti ₂ B ₂ O ₂	-2.720	-2.733	-2.693	-2.623
Na _x Ti ₂ C	4.406	2.519	1.276	0.898
Na _x Ti ₂ B ₂	6.865	2.865	1.633	1.095
Na _x Ti ₂ B ₂ H ₂	3.129	1.394	1.028	0.910
Na _x Ti ₂ B ₂ H ₄	1.135	-1.197	0.051	0.030
Na _x Ti ₂ B ₂ O ₂	-2.578	-2.545	-2.379	-2.178

2D Ti₂B₂ material has similar properties to that of 2D Ti₂C. The positive intercalation energies show that there is a strong binding energy between the two Ti₂B₂ monolayers. When the surface of Ti₂B₂ is covered with a layer of H (Ti₂B₂H₂), the intercalation energies of Li/Na decrease obviously, which is due to the decrease of the binding energy between the two Ti₂B₂H₂ monolayers. For the Ti₂B₂H₄ bilayer, the Li_{0.25}Ti₂B₂H₄, Li_{0.375}Ti₂B₂H₄, Li_{0.5}Ti₂B₂H₄, and Na_{0.25}Ti₂B₂H₄ compounds exhibit negative intercalation energies, while the other compounds in Table 3 show positive intercalation energies. The intercalation energies of Li/Na in the bilayer of Ti₂B₂O₂ are all negative, showing the favorability of Li/Na insertion into the Ti₂B₂O₂ bilayer. In our next work, we will discuss in detail the storage properties of Li/Na on 2D Ti₂B₂ with various surface functional groups.

4. Conclusion

Searching for suitable electrode materials with good performance is urgently needed for energy storage. In this work, we firstly reported a series of hexagonal 2D transition metal borides (TMBs) including Sc₂B₂, Ti₂B₂, V₂B₂, Cr₂B₂, Y₂B₂, Zr₂B₂, and Mo₂B₂ by using the first-principles method and crystal structure prediction techniques. Through the calculated phonon spectra and DOS, we confirmed that these TMBs possess great stability and excellent electronic conductivity.

Then, we investigated the potential of 2D Ti₂B₂ monolayer as an anode material for LIBs and NIBs on the basis of first-principles simulations. The Ti₂B₂ monolayer shows negative adsorption energies for Li and Na of -0.674 and -0.879 eV, respectively, on the most stable S1 site. The calculated theoretical specific capacity value for Li on Ti₂B₂ monolayer is 456 mA h g⁻¹, which is larger than that of well-established graphite, phosphorene, and Ti₃C₂. The theoretical specific capacity for Na was found to be 342 mA h g⁻¹, which is larger than that of MoS₂ and Mo₂C. More excitingly, we found that the Ti₂B₂ monolayer shows very high Li and Na diffusivity with an ultralow energy barrier of 0.017 and 0.008 eV, respectively, indicating an excellent charge-discharge capability for Li and Na. Moreover, the Ti₂B₂ monolayer was found to exhibit a metallic nature after the adsorption of Li and Na ions at any concentration, indicating that the Ti₂B₂ monolayer possesses an excellent electronic conductivity. Finally, the Ti₂B₂ monolayer shows just a small change

in volume after the adsorption of one, two, and three layers of Li and Na ions, indicating the robustness of this material.

Considering the above advantages, it is expected that Ti_2B_2 monolayer as well as the other hexagonal 2D TMBs could be used as anode materials for LIBs and NIBs with high specific capacity and fast diffusivity.

Conflicts of interest

The authors declare no competing financial interest.

Acknowledgements

F. W. W. and J. R. Z. acknowledge financial support from the National Natural Science Foundation of China under Grants No. 11675255, No. 11634008, and No. 11675195. J. R. Z. acknowledges financial support from the National Key Basic Research Program under Grants No. 2017YFA0403700. The calculations were performed at the Supercomputer Centre in the China Spallation Neutron Source.

References

- 1 J. R. Miller, *Science*, 2012, **335**, 1312–1313.
- 2 A. S. Aricò, P. Bruce, B. Scrosati, J.-M. Tarascon and W. van Schalkwijk, *Nat. Mater.*, 2005, **4**, 366–377.
- 3 M. Armand and J. M. Tarascon, *Nature*, 2008, **451**, 652–657.
- 4 D. P. Dubal, O. Ayyad, V. Ruiz and P. Gomez-Romero, *Chem. Soc. Rev.*, 2015, **44**, 1777–1790.
- 5 Y. Idota, T. Kubota, A. Matsufuji, Y. Maekawa and T. Miyasaka, *Science*, 1997, **276**, 1395–1397.
- 6 N. Oyama, T. Tatsuma, T. Sato and T. Sotomura, *Nature*, 1995, **373**, 598–600.
- 7 P. Simon, Y. Gogotsi and B. Dunn, *Science*, 2014, **343**, 1210–1211.
- 8 J. M. Tarascon and M. Armand, *Nature*, 2001, **414**, 359–367.
- 9 M. S. Whittingham, *Science*, 1976, **192**, 1126–1127.
- 10 Y. Wang, B. Liu, Q. Li, S. Cartmell, S. Ferrara, Z. D. Deng and J. Xiao, *J. Power Sources*, 2015, **286**, 330–345.
- 11 A. Barré, B. Deguilhem, S. Grolleau, M. Gérard, F. Suard and D. Riu, *J. Power Sources*, 2013, **241**, 680–689.
- 12 W. Luo, F. Shen, C. Bommier, H. Zhu, X. Ji and L. Hu, *Acc. Chem. Res.*, 2016, **49**, 231–240.
- 13 N. Yabuuchi, K. Kubota, M. Dahbi and S. Komaba, *Chem. Rev.*, 2014, **114**, 11636–11682.
- 14 H. Pan, Y.-S. Hu and L. Chen, *Energy Environ. Sci.*, 2013, **6**, 2338–2360.
- 15 M. D. Slater, D. Kim, E. Lee and C. S. Johnson, *Adv. Funct. Mater.*, 2013, **23**, 947–958.
- 16 Y. Wang, R. Chen, T. Chen, H. Lv, G. Zhu, L. Ma, C. Wang, Z. Jin and J. Liu, *Energ. Storage Mater.*, 2016, **4**, 103–129.
- 17 R. Zhao, J. Liu and J. Gu, *Appl. Energy*, 2015, **139**, 220–229.
- 18 Y. Lee, B. Son, J. Choi, J. H. Kim, M.-H. Ryoo and Y. M. Lee, *J. Power Sources*, 2015, **275**, 712–719.
- 19 M. Endo, C. Kim, K. Nishimura, T. Fujino and K. Miyashita, *Carbon*, 2000, **38**, 183–197.
- 20 J. R. Dahn, T. Zheng, Y. Liu and J. S. Xue, *Science*, 1995, **270**, 590–593.
- 21 M. Winter, J. O. Besenhard, M. E. Spahr and P. Novák, *Adv. Mater.*, 1998, **10**, 725–763.
- 22 D. P. DiVincenzo and E. J. Mele, *Phys. Rev. B: Condens. Matter Mater. Phys.*, 1985, **32**, 2538–2553.
- 23 S. Meini, R. Elazari, A. Rosenman, A. Garsuch and D. Aurbach, *J. Phys. Chem. Lett.*, 2014, **5**, 915–918.
- 24 D. Takamatsu, T. Nakatsutsumi, S. Mori, Y. Orikasa, M. Mogi, H. Yamashige, K. Sato, T. Fujimoto, Y. Takanashi, H. Murayama, M. Oishi, H. Tanida, T. Uruga, H. Arai, Y. Uchimoto and Z. Ogumi, *J. Phys. Chem. Lett.*, 2011, **2**, 2511–2514.
- 25 K. Song, D.-H. Seo, M. R. Jo, Y.-I. Kim, K. Kang and Y.-M. Kang, *J. Phys. Chem. Lett.*, 2014, **5**, 1368–1373.
- 26 W. Sun, Y. Li, B. Wang, X. Jiang, M. I. Katsnelson, P. Korzhavyi, O. Eriksson and I. Di Marco, *Nanoscale*, 2016, **8**, 15753–15762.
- 27 P. F. Liu, Y. Wu, T. Bo, L. Hou, J. Xu, H. J. Zhang and B. T. Wang, *Phys. Chem. Chem. Phys.*, 2018, **20**, 732–737.
- 28 Q. Kong, W. Feng, Q. Wang, L. Y. Gan and C. Sun, *Phys. Chem. Chem. Phys.*, 2017, **19**, 8563–8567.
- 29 D. Das, R. P. Hardikar, S. S. Han, K.-R. Lee and A. K. Singh, *Phys. Chem. Chem. Phys.*, 2017, **19**, 24230–24239.
- 30 A. Gupta, T. Sakthivel and S. Seal, *Prog. Mater. Sci.*, 2015, **73**, 44–126.
- 31 H. R. Jiang, Z. Lu, M. C. Wu, F. Ciucci and T. S. Zhao, *Nano Energy*, 2016, **23**, 97–104.
- 32 C. Eames and M. S. Islam, *J. Am. Chem. Soc.*, 2014, **136**, 16270–16276.
- 33 Q. Tang, Z. Zhou and P. Shen, *J. Am. Chem. Soc.*, 2012, **134**, 16909–16916.
- 34 Y. Xie, M. Naguib, V. N. Mochalin, M. W. Barsoum, Y. Gogotsi, X. Yu, K. W. Nam, X. Q. Yang, A. I. Kolesnikov and P. R. Kent, *J. Am. Chem. Soc.*, 2014, **136**, 6385–6394.
- 35 D. Er, J. Li, M. Naguib, Y. Gogotsi and V. B. Shenoy, *ACS Appl. Mater. Interfaces*, 2014, **6**, 11173–11179.
- 36 J. Hu, B. Xu, S. A. Yang, S. Guan, C. Ouyang and Y. Yao, *ACS Appl. Mater. Interfaces*, 2015, **7**, 24016–24022.
- 37 N. K. Jena, R. B. Araujo, V. Shukla and R. Ahuja, *ACS Appl. Mater. Interfaces*, 2017, **9**, 16148–16158.
- 38 H. R. Jiang, W. Shyy, M. Liu, L. Wei, M. C. Wu and T. S. Zhao, *J. Mater. Chem. A*, 2017, **5**, 672–679.
- 39 J. Liu, T. Zhao, S. Zhang and Q. Wang, *Nano Energy*, 2017, **38**, 263–270.
- 40 Q. Sun, Y. Dai, Y. Ma, T. Jing, W. Wei and B. Huang, *J. Phys. Chem. Lett.*, 2016, **7**, 937–943.
- 41 D. Wang, Y. Gao, Y. Liu, D. Jin, Y. Gogotsi, X. Meng, F. Du, G. Chen and Y. Wei, *J. Phys. Chem. C*, 2017, **121**, 13025–13034.
- 42 Y. Zhou and X. Zu, *Electrochim. Acta*, 2017, **235**, 167–174.
- 43 L. Dong, H. Kumar, B. Anasori, Y. Gogotsi and V. B. Shenoy, *J. Phys. Chem. Lett.*, 2017, **8**, 422–428.
- 44 R. P. Joshi, B. Ozdemir, V. Barone and J. E. Peralta, *J. Phys. Chem. Lett.*, 2015, **6**, 2728–2732.
- 45 Q. Peng, Z. Wang, B. Sa, B. Wu and Z. Sun, *ACS Appl. Mater. Interfaces*, 2016, **8**, 13449–13457.

- 46 Q. Peng, K. Hu, B. Sa, J. Zhou, B. Wu, X. Hou and Z. Sun, *Nano Res.*, 2017, **10**, 3136–3150.
- 47 Y. Zhang, Z. F. Wu, P. F. Gao, S. L. Zhang and Y. H. Wen, *ACS Appl. Mater. Interfaces*, 2016, **8**, 22175–22181.
- 48 Y. Li, F. Ma and L.-W. Wang, *J. Mater. Chem. A*, 2018, **6**, 7815–7826.
- 49 M. Liang and L. Zhi, *J. Mater. Chem.*, 2009, **19**, 5871–5878.
- 50 G. Kucinskis, G. Bajars and J. Kleperis, *J. Power Sources*, 2013, **240**, 66–79.
- 51 M. Mortazavi, C. Wang, J. Deng, V. B. Shenoy and N. V. Medhekar, *J. Power Sources*, 2014, **268**, 279–286.
- 52 Y. Jing, Z. Zhou, C. R. Cabrera and Z. Chen, *J. Phys. Chem. C*, 2013, **117**, 25409–25413.
- 53 G. A. Tritsaris, E. Kaxiras, S. Meng and E. Wang, *Nano Lett.*, 2013, **13**, 2258–2263.
- 54 R. Zhang, X. Wu and J. Yang, *Nanoscale*, 2016, **8**, 4001–4006.
- 55 W. Li, Y. Yang, G. Zhang and Y.-W. Zhang, *Nano Lett.*, 2015, **15**, 1691–1697.
- 56 V. V. Kulish, O. I. Malyi, C. Persson and P. Wu, *Phys. Chem. Chem. Phys.*, 2015, **17**, 13921–13928.
- 57 P. Liang, Y. Cao, B. Tai, L. Zhang, H. Shu, F. Li, D. Chao and X. Du, *J. Alloys Compd.*, 2017, **704**, 152–159.
- 58 M. Naguib, O. Mashtalir, J. Carle, V. Presser, J. Lu, L. Hultman, Y. Gogotsi and M. W. Barsoum, *ACS Nano*, 2012, **6**, 1322–1331.
- 59 M. Naguib, M. Kurtoglu, V. Presser, J. Lu, J. Niu, M. Heon, L. Hultman, Y. Gogotsi and M. W. Barsoum, *Adv. Mater.*, 2011, **23**, 4248–4253.
- 60 J. Halim, S. Kota, M. R. Lukatskaya, M. Naguib, M.-Q. Zhao, E. J. Moon, J. Pitock, J. Nanda, S. J. May, Y. Gogotsi and M. W. Barsoum, *Adv. Funct. Mater.*, 2016, **26**, 3118–3127.
- 61 K. Wang, Y. Zhou, W. Xu, D. Huang, Z. Wang and M. Hong, *Ceram. Int.*, 2016, **42**, 8419–8424.
- 62 A. Mishra, P. Srivastava, H. Mizuseki, K.-R. Lee and A. K. Singh, *Phys. Chem. Chem. Phys.*, 2016, **18**, 11073–11080.
- 63 M. Naguib and Y. Gogotsi, *Acc. Chem. Res.*, 2015, **48**, 128–135.
- 64 Z. Guo, J. Zhou and Z. Sun, *J. Mater. Chem. A*, 2017, **5**, 23530–23535.
- 65 S. Ma, K. Bao, Q. Tao, C. Xu, X. Feng, P. Zhu and T. Cui, *Inorg. Chem.*, 2016, **55**, 11140–11146.
- 66 S.-Y. Xie, X.-B. Li, W. Q. Tian, N.-K. Chen, X.-L. Zhang, Y. Wang, S. Zhang and H.-B. Sun, *Phys. Rev. B: Condens. Matter Mater. Phys.*, 2014, **90**, 035447.
- 67 Y. Wang, J. Lv, L. Zhu and Y. Ma, *Phys. Rev. B: Condens. Matter Mater. Phys.*, 2010, **82**, 094116.
- 68 Y. Wang, M. Miao, J. Lv, L. Zhu, K. Yin, H. Liu and Y. Ma, *J. Chem. Phys.*, 2012, **137**, 224108.
- 69 Y. Wang, J. Lv, L. Zhu and Y. Ma, *Comput. Phys. Commun.*, 2012, **183**, 2063–2070.
- 70 G. Kresse and J. Furthmüller, *Phys. Rev. B: Condens. Matter Mater. Phys.*, 1996, **54**, 11169–11186.
- 71 G. Kresse and J. Furthmüller, *Comput. Mater. Sci.*, 1996, **6**, 15–50.
- 72 G. Kresse and J. Hafner, *Phys. Rev. B: Condens. Matter Mater. Phys.*, 1993, **47**, 558–561.
- 73 Z. Guo, J. Zhou, C. Si and Z. Sun, *Phys. Chem. Chem. Phys.*, 2015, **17**, 15348–15354.
- 74 B. Anasori, M. R. Lukatskaya and Y. Gogotsi, *Nat. Rev. Mater.*, 2017, **2**, 16098.
- 75 B. T. Wang, P. Zhang, H. L. Shi, B. Sun and W. D. Li, *Eur. Phys. J. B*, 2010, **74**, 303–308.
- 76 S. Otani and Y. Ishizawa, *J. Cryst. Growth*, 1994, **140**, 451–453.
- 77 H. Klesnar, T. L. Aselage, B. Morosin and G. H. Kwei, *J. Alloys Compd.*, 1996, **241**, 180–186.
- 78 H. P. Klesnar and P. Rogl, *High Temp. – High Pressures*, 1990, **22**, 453–457.
- 79 L. N. Kugai, *Inorg. Mater.*, 1972, **4**, 669–670.
- 80 B.-T. Wang, W. Zhang and W.-D. Li, *Sci. Adv. Mater.*, 2013, **5**, 1916–1921.
- 81 G. Levchenko, A. Lyashchenko, V. Baumer, A. Evdokimova, V. Filippov, Y. Paderno and N. Shitsevalova, *J. Solid State Chem.*, 2006, **179**, 2949–2953.
- 82 H. Zhang, Y. Li, J. Hou, A. Du and Z. Chen, *Nano Lett.*, 2016, **16**, 6124–6129.
- 83 Z. Zhang, X. Liu, B. I. Yakobson and W. Guo, *J. Am. Chem. Soc.*, 2012, **134**, 19326–19329.
- 84 L. M. Yang, V. Bacic, I. A. Popov, A. I. Boldyrev, T. Heine, T. Frauenheim and E. Ganz, *J. Am. Chem. Soc.*, 2015, **137**, 2757–2762.
- 85 A. Molina-Sánchez and L. Wirtz, *Phys. Rev. B: Condens. Matter Mater. Phys.*, 2011, **84**, 155413.
- 86 H. Liu, A. T. Neal, Z. Zhu, Z. Luo, X. Xu, D. Tománek and P. D. Ye, *ACS Nano*, 2014, **8**, 4033–4041.
- 87 K. F. Mak, C. Lee, J. Hone, J. Shan and T. F. Heinz, *Phys. Rev. Lett.*, 2010, **105**, 136805.
- 88 K. Toyoura, Y. Koyama, A. Kuwabara, F. Oba and I. Tanaka, *Phys. Rev. B: Condens. Matter Mater. Phys.*, 2008, **78**, 214303.
- 89 P. Ganesh, J. Kim, C. Park, M. Yoon, F. A. Reboreda and P. R. C. Kent, *J. Chem. Theory Comput.*, 2014, **10**, 5318–5323.
- 90 W.-J. Zhang, *J. Power Sources*, 2011, **196**, 13–24.
- 91 W. Wenhui, Z. Qianfan, C. Yi and W. Enge, *J. Phys.: Condens. Matter*, 2010, **22**, 415501.
- 92 C.-Y. Chou, H. Kim and G. S. Hwang, *J. Phys. Chem. C*, 2011, **115**, 20018–20026.
- 93 K. Nakada and A. Ishii, *Solid State Commun.*, 2011, **151**, 13–16.
- 94 C. Ling and F. Mizuno, *Phys. Chem. Chem. Phys.*, 2014, **16**, 10419–10424.
- 95 B. Ziebarth, M. Klinsmann, T. Eckl and C. Elsässer, *Phys. Rev. B: Condens. Matter Mater. Phys.*, 2014, **89**, 174301.
- 96 X. Qu, J. Yang, Y. Wang, J. Lv, Z. Chen and Y. Ma, *Nanoscale*, 2017, **9**, 17983–17990.